

Article

The Energy Dissipation, AE Characteristics, and Microcrack Evolution of Rock–Backfill Composite Materials (RBCM)

Jie Wang^{1,2,*}, Chi Zhang^{1,2,*}, Weidong Song^{1,2} and Yongfang Zhang^{1,2}

¹ State Key Laboratory of High-Efficient Mining and Safety of Metal Mines of Ministry of Education, University of Science and Technology Beijing, Beijing 100083, China; songwd@ustb.edu.cn (W.S.); b1903098@ustb.edu.cn (Y.Z.)

² School of Civil and Resources Engineering, University of Science and Technology Beijing, Beijing 100083, China

* Correspondence: 18810582761@163.com (J.W.); zhangchi9531@163.com (C.Z.)

Abstract: The backfill in the stope usually forms a composite structure with the surrounding rock in order to bear pressure together to support the goaf and ensure the safe mining of subsequent ores. Based on laboratory tests and theoretical analysis, the energy and damage evolution of the rock–backfill composite materials (RBCM) are studied deeply. The results show that: (1) The σ_p (peak stress), ε_p (peak strain), and E (elasticity modulus) decreased with the increase of the internal backfill diameter. When the diameter of the backfill increases from 10 mm to 40 mm, σ_p decreases from 50.15 MPa to 18.14 MPa, ε_p decreases from 1.246% to 1.017%, and E decreases from 7.51 GPa to 2.33 GPa. The U^T shows an S-shaped distribution, the U^E shows an inverted U-shaped distribution, and the U^D first increases slowly and then increases rapidly. The U^T_p , U^E_p , U^D_p , U^E_p/U^D_p , and U^E_p/U^T_p decrease by 67.38%, 97.20%, 58.56%, 32.64% and 13.64% respectively, and the U^D_p/U^T_p increases by 20.93% with the increases of the backfill diameter. (2) A damage constitutive model of the RBCM is established based on the energy consumption characteristics. The damage evolution curve shows an S-shaped distribution, and the damage rate evolution curve shows an inverted U-shaped distribution. (3) The AE correlation fractal dimension decreases with the increase of the strain gradient and damage value, and the AE correlation fractal dimension presents linear and exponential functions with them, respectively. With the increase of stress, microcracks first appear and gather in the internal backfill of the RBCM, and then microcracks appear and gather in the peripheral rock, which together lead to the macro penetration failure of the RBCM.

Keywords: rock–backfill composite materials (RBCM); energy dissipation mechanism; damage constitutive model; microcrack evolution



Citation: Wang, J.; Zhang, C.; Song, W.; Zhang, Y. The Energy Dissipation, AE Characteristics, and Microcrack Evolution of Rock–Backfill Composite Materials (RBCM). *Minerals* **2022**, *12*, 482. <https://doi.org/10.3390/min12040482>

Academic Editor: Abbas Taheri

Received: 17 March 2022

Accepted: 12 April 2022

Published: 14 April 2022

Publisher's Note: MDPI stays neutral with regard to jurisdictional claims in published maps and institutional affiliations.



Copyright: © 2022 by the authors. Licensee MDPI, Basel, Switzerland. This article is an open access article distributed under the terms and conditions of the Creative Commons Attribution (CC BY) license (<https://creativecommons.org/licenses/by/4.0/>).

1. Introduction

The filling mining method involves mixing the tailings solid waste produced by ore mining with cement and other cementing agents, and transporting it to the underground goaf through pipelines. Therefore, its safety is significantly improved, and it has green and environmentally protective characteristics, which are widely used in metal mines at home and abroad, and there is an increasing trend of its use [1–6]. The stope is divided into the one-step room and the two-step pillar. The room is mined first, then the goaf is filled with cemented paste backfill, and then the pillar is mined. In this way, the pillar is mined under the support of the composite structure composed of cemented paste backfill and the surrounding rock. Therefore, the stability of the composite structure of the backfill and surrounding rock is the premise of safe pillar mining. Based on the above reasons, the stability of the pressure-bearing mechanism composed of cemented paste backfill and the surrounding rock must be analyzed in order to ensure safety in the whole pillar mining process.

Fruitful research results have been obtained regarding the stability research of intact rock and backfill [7–13], which not only greatly promoted the development and progress of mine rock mechanics and backfill mechanics but also laid a solid theoretical foundation for future generations to carry out relevant scientific research. Unlike the intact rock and backfill, the RBCM is composed of two different materials, in which the rock is a strong structure and the backfill is a weak structure. Under the load, the two structures interact and depend on each other to jointly resist the external load, and their mechanical properties and damage evolution mechanism will become very complex. However, at present, the research on the bearing mechanism of the rock–backfill composite structure is relatively sparse, but it has gradually attracted the attention of scholars [14–16]. Wang et al. [17] studied the influence of interface roughness and inclination on the strength and failure mode of the rock–backfill composite model. Wu et al. [18] suggested that the failure of the backfill–rock combination was largely caused by the shear failure of the interface. Xiu et al. [19] reported that the dry and wet degree of the interface between the rock and backfill had an important impact on the stability of the interface. Zhao et al. [20] introduced the KCC model, and comprehensively analyzed the influence of backfill inclination on damage initiation and propagation. Yu et al. [21] conducted a triaxial compression test on rock–backfill samples, and CT scanned the samples before and after compression to explore the role of the interface. The lack of basic theoretical research on the rock–backfill composite structure greatly limits its effective application in engineering.

In the process of the compression failure of rock, backfill, and other materials, internal cracks gradually sprout and expand, and release energy in the form of AE. The energy evolution mechanism and the AE characteristic parameters can characterize the damage process to a certain extent. Therefore, there is important significance in the study of the energy consumption and AE characteristics of materials in order to master their damage and instability mechanism [11,22–25]. Hou et al. [26] revealed the influence of the curing age on the energy dissipation characteristics of CPB. Wang et al. [27,28] carried out a triaxial compression test on CPB with different layers, and discussed the influence law of layered numbers and confining pressure on elastic energy and dissipation energy. With the help of numerical technology, Xin et al. [29] studied the influence of waste rock content on the energy evolution characteristics of CPB, and considered that the compressive and tensile energy absorbed by CPB decreased and the interface transition region increased with the increase of waste rock content. Zhao et al. [30] obtained the AE parameter curve by carrying out the uniaxial compression AE test, and deeply studied the change characteristics of the AE correlation fractal dimension during the compression failure of CPB with the help of fractal theory. Zhou et al. [31] deduced the AE energy fractal dimension based on the AE energy counting characteristics, and analyzed the internal relationship between the AE energy fractal dimension and the damage variable. He et al. [32] made rock–backfill combination models and discussed the influence of the cement–tailings ratio on the AE correlation fractal dimension of the combination model.

The failure and instability of CPB and other materials under compression is essentially a process of continuous damage accumulation. In order to understand the damage and instability mechanism of CPB materials, it is very important to establish a reasonable and reliable damage evolution model. Wang et al. [33] obtained the basic mechanical parameters of rock-encased backfill (REB), constructed the damage constitutive model of REB, and deeply discussed the damage evolution mechanism. Ma et al. [34] conducted numerical simulation research on the coal–rock composite structure, established the damage constitutive model of a coal–rock composite structure based on energy consumption theory, and discussed the damage evolution law. Liu et al. [35] studied the damage evolution characteristics of backfill at different temperatures, and considered that the damage evolution process of backfill can be divided into four stages: the nondestructive stage, the initial damage stage, the accelerated damage stage, and the stable damage stage. Cui et al. [36] developed an evolutive elasto-plastic model, and established a damage constitutive model of cemented backfill based on this model; the important role of cemented hydrate in its

damage evolution was studied. Sun et al. [12] introduced the disturbance element, connected Burges model, nonlinear viscous damper, and strain trigger, and established the creep disturbance constitutive model of backfill. Scholars have also established many other damage constitutive models of backfill [37–40]. These model construction ideas provide a great reference for the derivation and construction of the damage evolution equation in this paper.

In this paper, a uniaxial compression AE monitoring test of rock–backfill composite materials (RBCM) with different backfill diameters is carried out. Firstly, the stress–strain behavior and mechanical properties of the RBCM are analyzed, and the internal functional relationship between the peak stress, peak strain, elastic modulus and backfill diameter is revealed. Secondly, the energy dissipation law, the AE correlation fractal dimension, the AE events' location characteristics, and the microcrack temporal and spatial evolution of the RBCM are deeply studied. Finally, the damage evolution equation is introduced, and a damage constitutive model of the RBCM is established.

2. Materials and Methods

2.1. Research Background

The room of the filling mining method was first stopped, and then the goaf was filled with tailings cementation. At this time, the cemented paste backfill was surrounded by the surrounding rock, and formed a composite structure (Figure 1) with the surrounding rock to bear pressure together to support the goaf and ensure the safety of the ore mining. Unlike the intact backfill and rock materials, the composite materials were formed by the mutual wrapping of two different media. Their mechanical properties, energy consumption mechanism, and damage evolution need to be further studied.

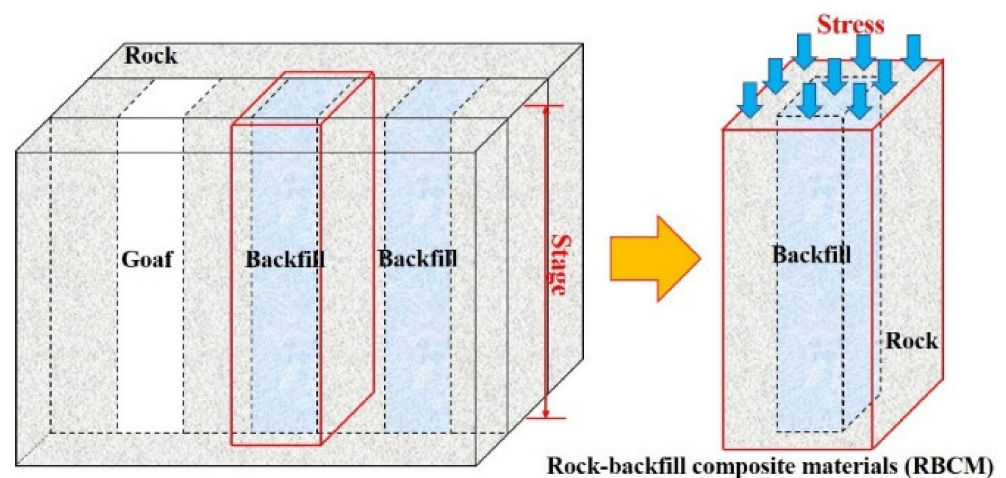


Figure 1. Field model of rock–backfill composite materials.

2.2. Materials

The tailings used for the cemented paste backfill were from a mine in Shandong Province, China, and ordinary Portland cement (OPC) 32.5R was used as a cementing agent. The PSD curve of the tailings was obtained using an LS-POP (9) laser particle size analyzer, as shown in Figure 2. Figure 3 shows the chemical composition of the tailings and OPC obtained by X-ray fluorescence.

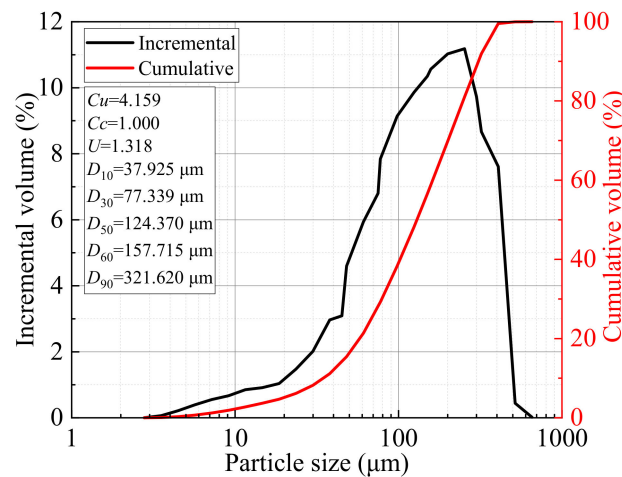


Figure 2. The PSD curves of the tailings.

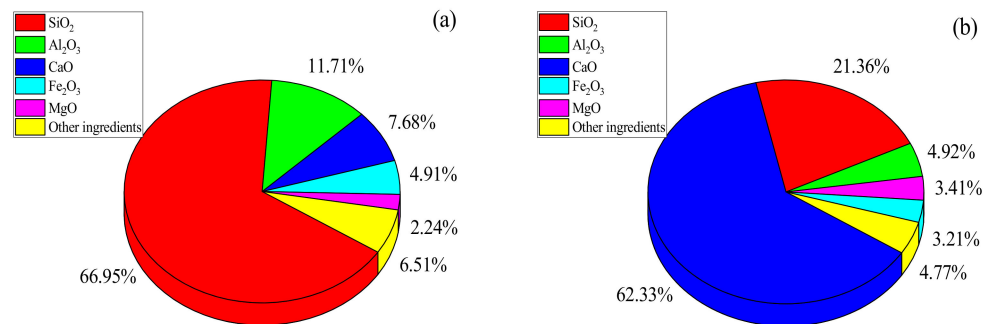


Figure 3. The chemical composition: (a) tailings; (b) OPC.

2.3. Test Scheme

In this paper, four different types of rock–backfill composite materials (RBCM) were designed and made. The complete rock center was hollowed out by drilling, and the internal backfill was prepared according to the designed ratio to fill the interior of the rock, which was preserved in a standard maintenance box to a specified age. According to the design requirements, the diameter of the peripheral rock was $d_r = 50$ mm and the height was $h_r = 100$ mm. The diameters of the internal backfill were $d_b = 10$ mm, 20 mm, 30 mm, and 40 mm respectively, and the height of the internal backfill was $h_b = 100$ mm. The test scheme and sample number are shown in Table 1. Each group prepares 3 samples, a total of 12 RBCM samples, and the RBCM samples designed and manufactured are shown in Figure 4.

Table 1. UCS and elastic modulus of different kinds of samples.

Sample ID	Backfill Diameter d_b (mm)	c/t Ratio	Peak Stress (MPa)	Peak Strain (%)	Elastic Modulus (GPa)
RBCM-10	10	1:4	50.15	1.246	7.51
RBCM-20	20		42.47	1.106	5.72
RBCM-30	30		28.73	1.040	3.88
RBCM-40	40		18.14	1.017	2.33

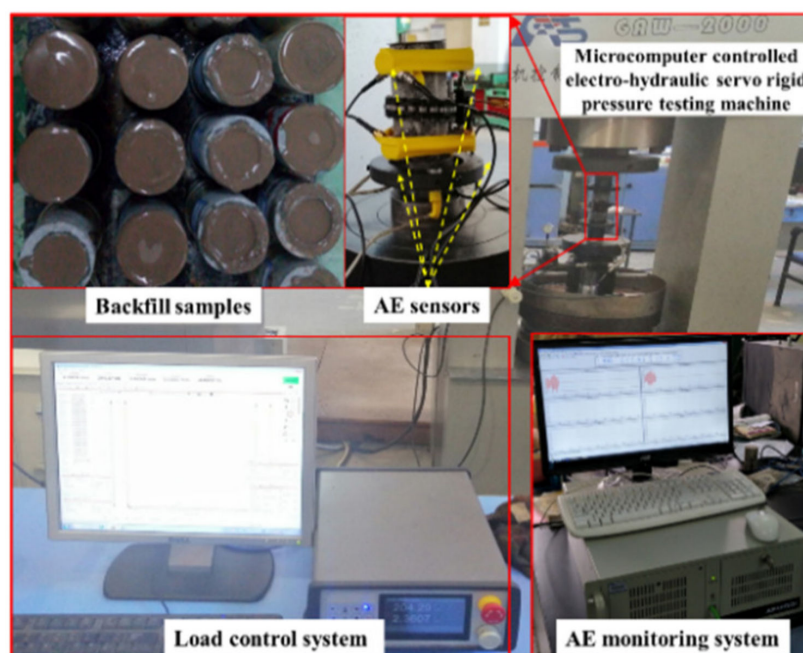


Figure 4. Uniaxial compressive AE test devices.

2.4. Test Devices

The Gaw-2000 system (Figure 4) was used to carry out uniaxial compression AE tests on the RBCM samples. The displacement control mode was adopted, and the loading rate was maintained at 0.5 mm/min. A PCI-2 AE monitoring system was adopted. A total of 6 sensors were used. The sensor frequency was 140 kHz and the noise threshold was set to 45 dB. The sensors' layout position is shown in Figure 4. During compression, the stress, strain, and AE data were recorded and exported in Excel format.

3. Results and Analysis

3.1. Mechanical Properties

Figure 5 shows the stress–strain curves of four RBCM samples. The curves can be divided into five different stages. Stage I: The internal pores and cracks of the RBCM are compacted and closed, the sample becomes denser, and the stress–strain curve is concave. Stage II: With the increase of stress, the cracks are almost all closed, the strain increases linearly, the RBCM produces elastic deformation, there is almost no new crack damage, and the stress–strain curve increases linearly. Stage III: The stress gradually exceeds the yield stress of the RBCM, the sample begins to produce plastic deformation, and new cracks and damage are generated; the stress–strain curve is concave, and the RBCM samples' strength begins to approach the peak. Stage IV: When the stress reaches and exceeds the bearing limit of the RBCM, many new cracks and damages sprout on the sample's surface, the macro failure begins to form, and the stress–strain curve reaches the peak and begins to decrease. Stage V: At this stage, the peripheral rocks gradually lose their bearing capacity, but due to the certain bearing capacity of the backfill wrapped in the center, the RBCM has residual stress. It slows down the rate of RBCM deformation and its complete failure, and some samples have double peaks; the stress–strain curve will extend slowly forward.

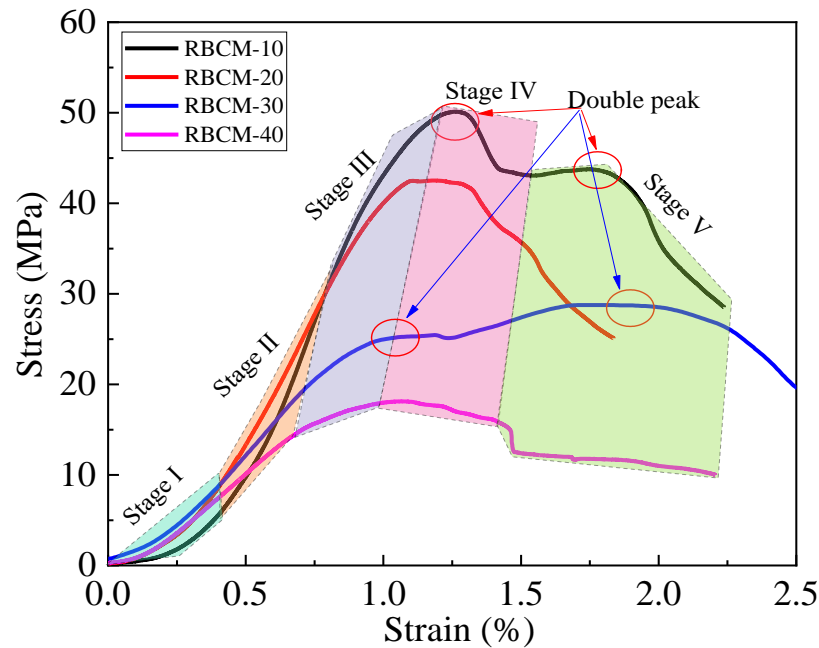


Figure 5. Stress–strain curves of the RBCM samples.

The mechanical properties of the RBCM are closely related to the size of the central backfill. Figure 6 shows the relationship between the peak stress σ_p , peak strain ϵ_p , elastic modulus E , and the backfill diameter of the RBCM. Figure 6a shows that the σ_p of the RBCM decreases with the increase of the backfill diameter. When the backfill diameter is 10 mm, the σ_p is 50.15 MPa. When the backfill diameter increases to 40 mm, the σ_p of the RBCM decreases to 18.14 MPa. Figure 6b shows that the ϵ_p of the RBCM also decreases with the increase of the backfill diameter. When the backfill diameter increases from 10 mm to 40 mm, the ϵ_p of the RBCM decreases from 1.246% to 1.017%. Figure 6c shows that the E of the RBCM also decreases with the increase of the backfill diameter. When the backfill diameter increases from 10 mm to 40 mm, the E decreases from 7.51 GPa to 2.33 GPa.

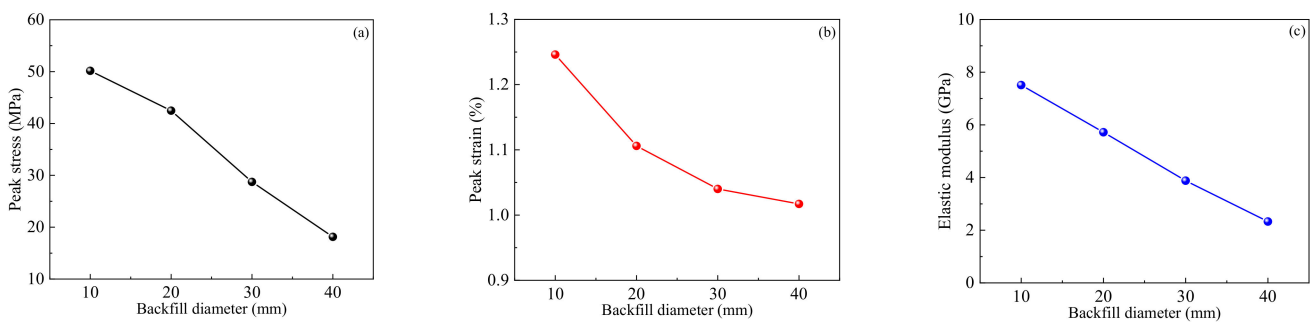


Figure 6. The relationship between the mechanical properties and backfill diameter: (a) the σ_p ; (b) the ϵ_p ; (c) the E .

3.2. Energy Dissipation Mechanisms

The essence of the deformation and failure of the RBCM under load is the process of the continuous input of external energy and conversion into elastic energy and dissipative energy. According to energy conservation [41,42]:

$$U^T = U^E + U^D \tag{1}$$

where U^T is the total energy input to the RBCM from the outside, and U^E and U^D are the releasable elastic energy and dissipative energy of the RBCM, respectively.

The total energy U^T absorbed by the RBCM from the outside under uniaxial compression can be expressed by the following formula:

$$U^T = \int_0^\epsilon \sigma d\epsilon \tag{2}$$

The release elastic energy U^E of the RBCM can be expressed by the following formula:

$$U^E = \frac{\sigma^2}{2\bar{E}} \tag{3}$$

where \bar{E} is unload elastic modulus of the RBCM.

According to Equations (1)–(3) and the stress–strain curves of the RBCM, the energy evolution law of the RBCM with different backfill diameters can be obtained. The results are shown in Figure 7.

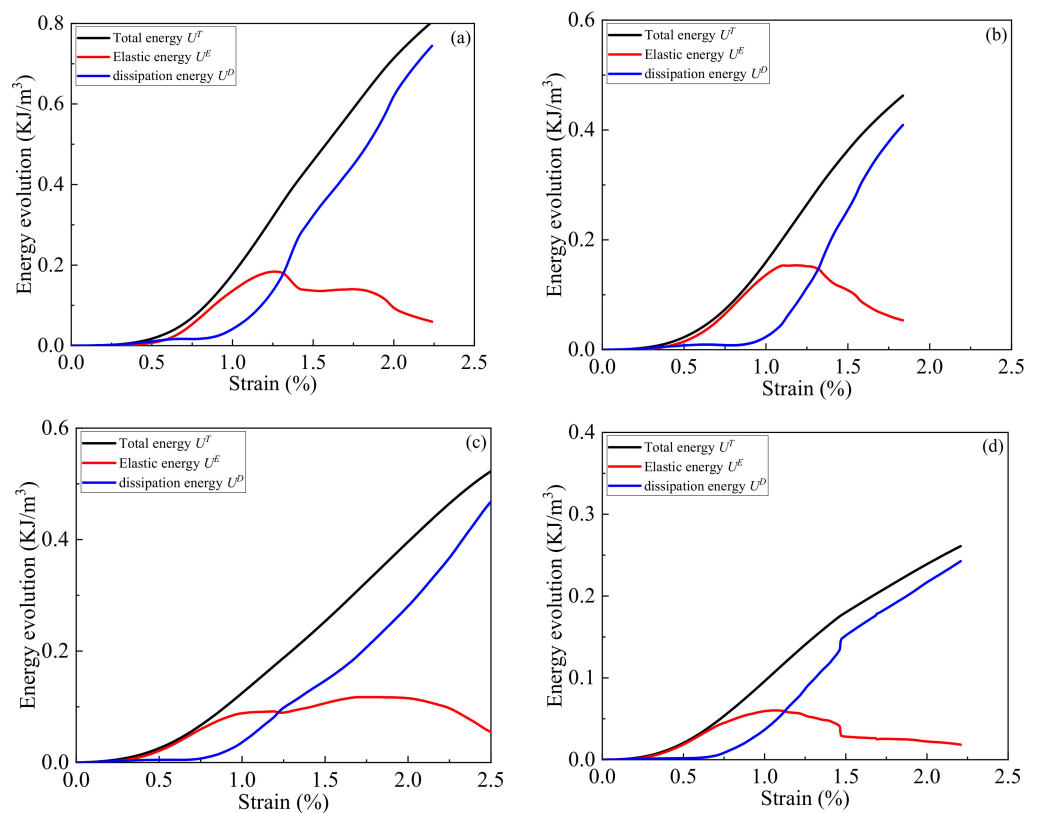


Figure 7. Energy evolution of the different samples: (a) RBCM-10; (b) RBCM-20; (c) RBCM-30; (d) RBCM-40.

Figure 7 shows that the total energy input to the RBCM is first converted into releasable elastic energy and stored in the sample, and the releasable elastic energy begins to increase (the red curve begins to rise). At this time, the sample only has elastic deformation, no damage and almost no energy dissipation. Then, the released elastic energy accumulates continuously and gradually exceeds the energy storage limit of the RBCM, the sample begins to produce damage and energy dissipation, and the dissipated energy begins to increase (the blue curve begins to rise). Finally, the released elastic energy decreases, and the dissipated energy increases rapidly until the sample is destroyed.

Figure 8 shows the energy evolution laws of the RBCM. Figure 8a shows that the total energy evolution curve of the input of the RBCM shows an S-shaped distribution. The black line is at the top, indicating that the RBCM-10 sample has the fastest total energy accumulation rate and the largest total energy. The pink line is at the bottom, indicating that

the RBCM-40 sample has the slowest total energy accumulation rate and the smallest total energy. Overall, the larger the backfill diameter, the slower the total energy accumulation rate and the smaller the total energy accumulation amount. Figure 8b shows that the releasable elastic energy stored in the RBCM first increases and then decreases, and the releasable elastic energy curve presents an inverted U-shaped distribution. The smaller the backfill diameter, the greater the energy storage limit of the RBCM. It can be seen from Figure 8c that the dissipated energy of the RBCM first increases slowly, and then increases rapidly until the sample is destroyed. The smaller the backfill diameter, the greater the energy dissipation of the RBCM.

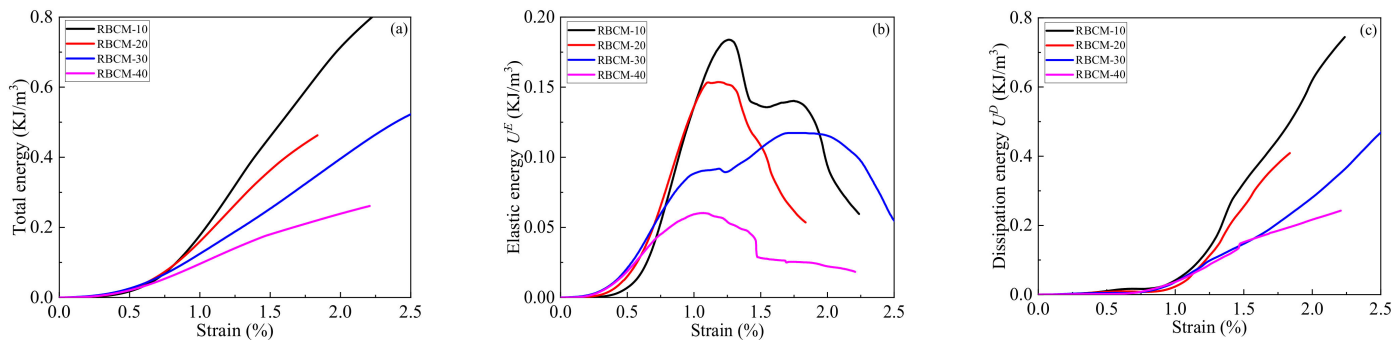


Figure 8. Different types of energy evolution: (a) total energy; (b) elastic energy; (c) dissipation energy.

Figure 9 and Table 2 show the relationship between different types of energy, the energy rate of the RBCM at the peak stress point, and the backfill diameter. Figure 9a shows that the released elastic energy at the peak point is greater than the dissipated energy. In addition, the total energy U^T_p input to the RBCM, the releasable elastic energy U^E_p stored in the RBCM, and the dissipation energy U^D_p all decrease with the increase of the backfill diameter. When the backfill diameter increases from 10 to 40 mm, the U^T_p , U^E_p , and U^D_p decrease from 0.325 kJ/m³ to 0.106 kJ/m³, from 0.214 kJ/m³ to 0.060 kJ/m³, and from 0.111 kJ/m³ to 0.046 kJ/m³, respectively. As can be seen from Figure 9b, the U^E_p/U^D_p and U^E_p/U^T_p decrease with the increase of the backfill diameter. When the backfill diameter increases from 10 to 40 mm, the U^E_p/U^D_p and U^E_p/U^T_p decrease from 1.93 to 1.30, and from 0.66 to 0.57, respectively. In addition, the U^D_p/U^T_p increases with the increase of the backfill diameter. When the backfill diameter increases from 10 to 40 mm, the U^D_p/U^T_p increases from 0.34 to 0.43.

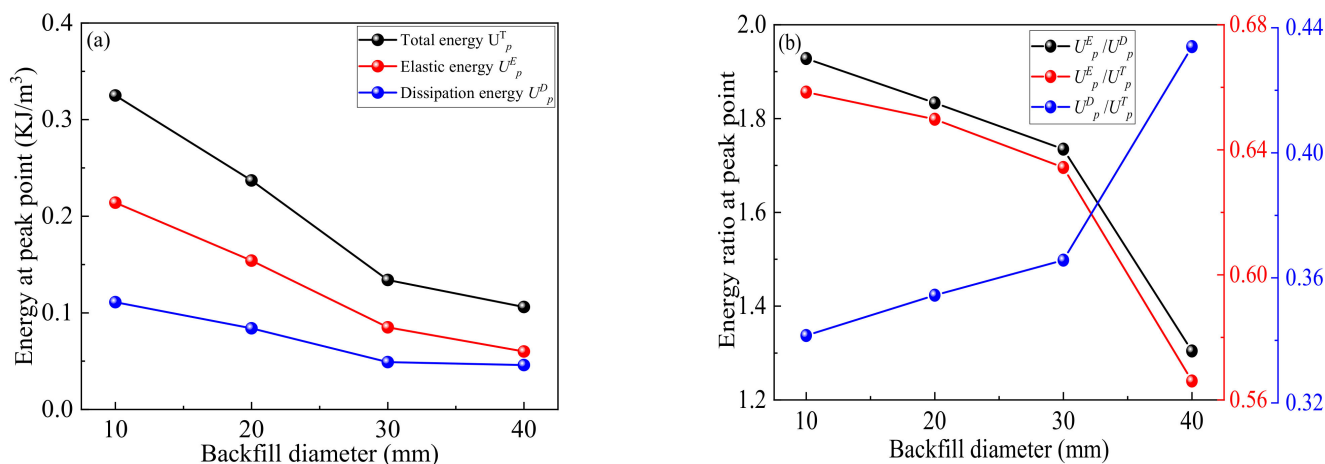


Figure 9. Energy and energy ratio at the peak point: (a) energy; (b) energy ratio.

Table 2. The U_p^T , U_p^E , and U_p^D of the RBCM at the peak stress point.

ID	RBCM-10	RBCM-20	RBCM-30	RBCM-40
U_p^T (KJ/m ³)	0.325	0.237	0.134	0.106
U_p^E (KJ/m ³)	0.214	0.154	0.085	0.06
U_p^D (KJ/m ³)	0.111	0.084	0.049	0.046
U_p^E/U_p^D	1.93	1.83	1.73	1.30
U_p^E/U_p^T	0.66	0.65	0.63	0.57
U_p^D/U_p^T	0.34	0.35	0.37	0.43

3.3. Damage Constitutive Model

3.3.1. Model Constructed

According to the energy dissipation characteristics of the coal–rock combination, Ma et al. [34] considered that all of the energy dissipation generated by materials under load is not used to produce damage, proposed a modified damage variable, and verified the rationality of the damage variable through experimental research:

$$D = (1 - \frac{\sigma_r}{\sigma_p}) \cdot \frac{U^D}{U_{max}^D} \cdot (1 + \frac{U_p^D}{U_p^T}) \tag{4}$$

where D is the damage variable of the RBCM, σ_r is the residual stress of the RBCM, σ_p is the peak stress of the RBCM, U^D is the dissipation energy, U_{max}^D is the cumulative dissipated energy, U_p^D is the dissipation energy at the peak point, and U_p^T is the total energy input to the RBCM at the peak point.

The damage constitutive model of the RBCM at uniaxial compression is

$$\sigma = (1 - D)E\varepsilon \tag{5}$$

$$\sigma = \left[1 - (1 - \frac{\sigma_r}{\sigma_p}) \cdot \frac{U^D}{U_{max}^D} \cdot (1 + \frac{U_p^D}{U_p^T}) \right] E\varepsilon \tag{6}$$

3.3.2. Model Validation

Figure 10 shows the comparison results between the test curve and the model curve. Figure 10a shows that the coincidence degree of the two curves is poor in the compaction closing stage, but the overall change trend is highly similar. Figure 10b–d show that the model curves are highly consistent with the sample curves.

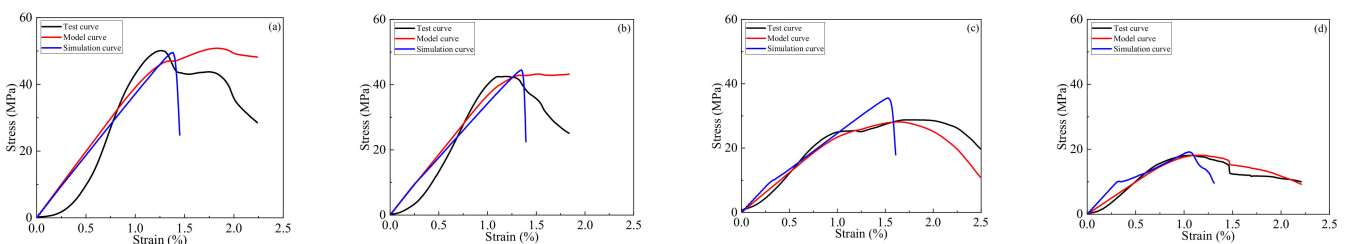


Figure 10. Comparison of the test, model, and simulation curves: (a) RBCM-10; (b) RBCM-20; (c) RBCM-30; (d) RBCM-40.

3.3.3. Damage Evolution Analysis

In order to analyze the damage evolution law of the RBCM under load, the damage evolution curves and damage rate evolution curves of the RBCM can be obtained according to Equation (4), and the results are shown in Figure 11. Figure 11a shows that, in the compaction and closing stage, the RBCM has almost no damage, and the damage curve extends forward close to the X-axis. In the linear elastic stage of the RBCM, only a small amount of damage occurs, and the damage curve rises slowly. After exceeding the yield

limit of the RBCM, the damage initiates and expands rapidly, and the damage curve rises rapidly. In general, the damage curve first extends horizontally forward, then rises slowly, and finally rises rapidly. Figure 11b shows that the damage rate evolution curves of the RBCM present an inverted U-shaped distribution, which first increases and then decreases. The results indicate that the damage accumulation rate of the RBCM first increases and then decreases.

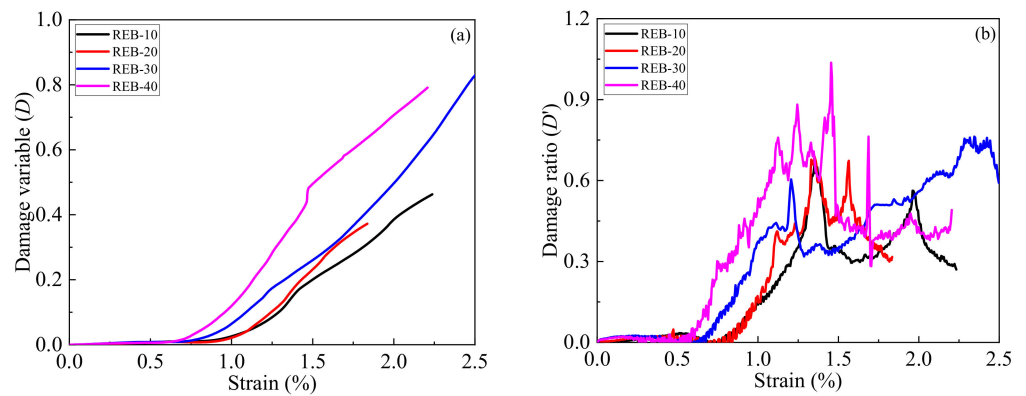


Figure 11. Damage and damage ratio evolution curves: (a) damage curve; (b) damage ratio curve.

3.4. AE Characteristics

3.4.1. AE Fractal Dimension

Fractal dimension is a parameter that quantitatively describes fractal characteristics and represents the complexity of the fractal body [43,44]. The correlation fractal dimension is used to describe the AE fractal characteristics of the RBCM in the failure process under uniaxial compression. The common calculation method of the correlation fractal dimension is the G-P algorithm. The G-P algorithm takes the AE parameter sequence as its research object, and each AE parameter sequence corresponds to a sequence set X_n with a capacity of n :

$$X_n = \{x_1, x_2 \cdots x_n\} \tag{7}$$

where x_i is the AE parameter, $i = 1, 2, \cdots n$. Take the first m points in Equation (8) to form the first m -dimensional vector space, which is recorded as

$$X_1 = \{x_1, x_2 \cdots x_m\} \tag{8}$$

Then move one point backward and take m points to form the second m -dimensional vector space. By analogy, Equation (7) can form a total of $N = n - m + 1$ m -dimensional vector spaces:

$$X = \begin{bmatrix} x_1 & x_2 & \cdots & x_m \\ x_2 & x_3 & \cdots & x_{m+1} \\ \vdots & \vdots & \cdots & \vdots \\ x_{n-m+1} & x_{n-m+2} & \cdots & x_n \end{bmatrix} \tag{9}$$

The correlation function $C(r)$ is

$$C(r) = \frac{1}{N^2} \sum_{i=1}^N \sum_{j=1}^N H(r - \|X_i - X_j\|) \tag{10}$$

where H is the Heaviside function, X_i and X_j are the i th and j th vector spaces respectively, and r is the given scale:

$$H(x) = \begin{cases} 1, & x > 0 \\ 0, & x \leq 0 \end{cases} \tag{11}$$

$$r = k \frac{1}{N^2} \sum_{i=1}^N \sum_{j=1}^N \|X_i - X_j\| \tag{12}$$

where k is coefficient. For a given r , there is always a corresponding correlation function $C(r)$. By substituting the $C(r)$ and r into the double logarithmic coordinate system, the coordinate points $(\lg C(r), \lg r)$ can be obtained. Taking different k values, respectively, multiple coordinate points can be obtained in the double logarithmic coordinate system. The obtained coordinate points are subjected to univariate linear regression, and the slope of the regression function is the AE correlation fractal dimension D_f .

Figure 12 shows the relationship curve between the AE ringing count correlation fractal dimension and the damage variable at different strain stages. With the increase of the strain, the AE correlation fractal dimension decreases, while the damage variable continues to increase. At the initial stage of loading, the internal microcracks of the RBCM are gradually compacted and closed, almost no damage is generated, the AE ringing counts evolve irregularly, and the correlation fractal dimension of the AE parameters is large. In the middle of loading, the internal crack began to evolve and expand gradually, the internal damage began to accumulate slowly, the AE ringing counts were released to the outside world according to a certain law, and the AE correlation fractal dimension gradually decreased. In the later stage of loading, the internal meso cracks evolve rapidly and become macro through failure, the internal damage accumulates rapidly, the AE ringing counts are released to the outside in an orderly manner, and the AE correlation fractal dimension is further reduced. This result is similar to the research results of Zhao [30] and Guo [43].

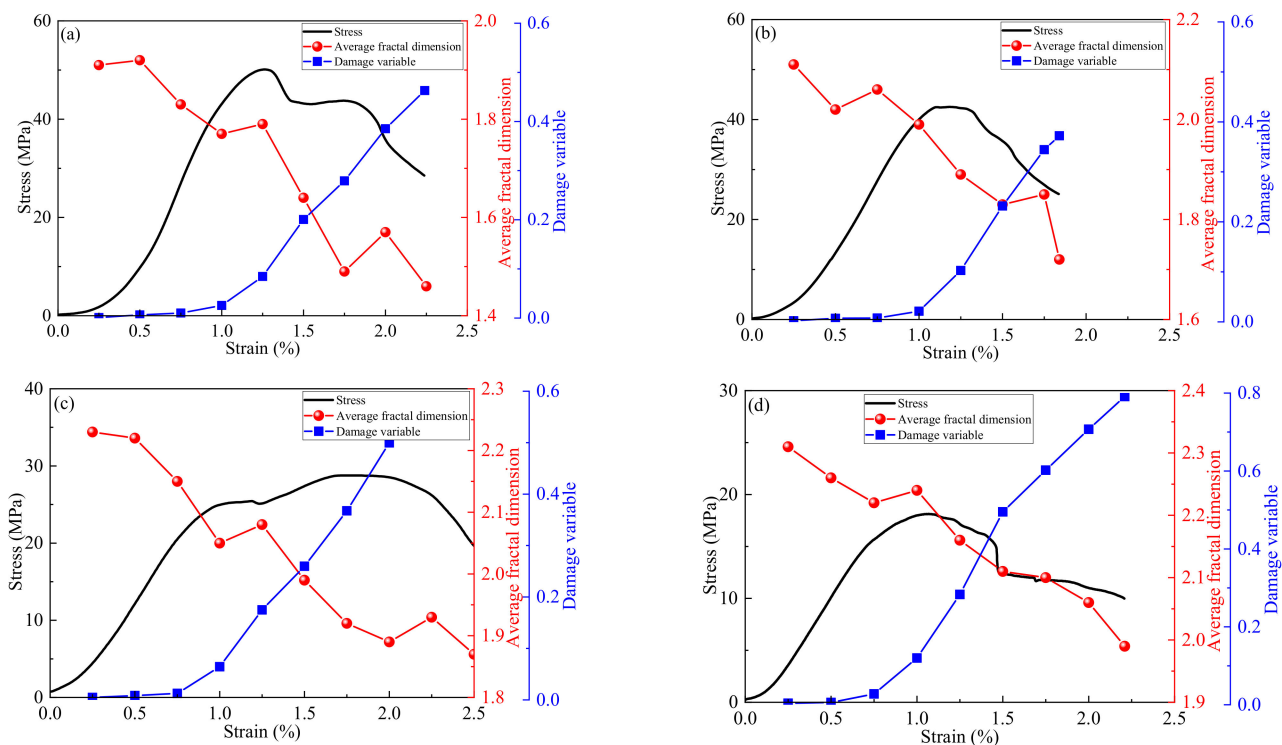


Figure 12. AE average fractal dimension: (a) RBCM-10; (b) RBCM-20; (c) RBCM-30; (d) RBCM-40.

3.4.2. AE Event Location

AE location technology can intuitively show the internal failure process of the RBCM. Figure 13 shows the AE event location of the RBCM-10 and RBCM-30. At the initial stage of loading (0%–30% ϵ_f), the internal cracks of the RBCM were closed by compression, and only a few AE events occurred in the internal backfill. With continuous loading (30%–50% ϵ_f), the internal cracks of the RBCM began to evolve gradually, the AE events began to increase gradually, and they mainly gathered in the internal backfill. When loading to 50%–80% ϵ_f ,

the cracks further increase, the AE events also increase, and they gradually appear in the external rock. When loading to 80%–100% ε_f , AE events begin to gather in the external rock, and macro penetration failure also occurs. At the later stage of loading (100%–120% ε_f), AE events do not increase significantly. Because the RBCM has not completely lost its bearing capacity, the macro crack will continue to expand, and a small number of AE events will appear in the external rock.

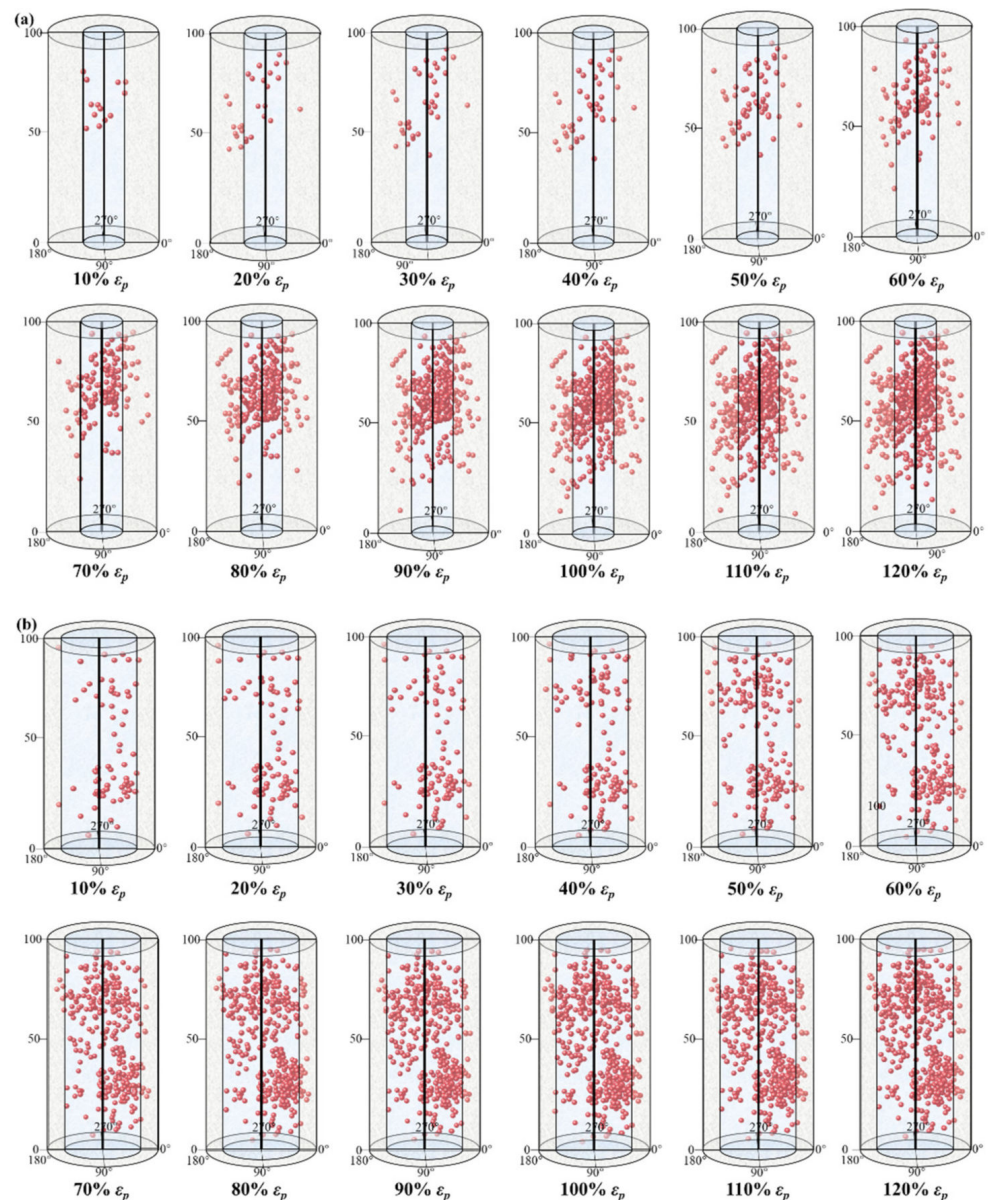


Figure 13. Temporal and spatial evolution of the AE events: (a) RBCM-10; (b) RBCM-30.

3.5. Temporal and Spatial Evolution of Microcracks

The laboratory test is the most direct means to study the internal damage evolution of the RBCM, but experimental research often cannot intuitively show the spatio-temporal evolution characteristics of internal cracks in the RBCM. At present, scholars at home and abroad often use Particle Flow Code (PFC) software to reveal the internal damage mechanism of materials. By establishing a numerical model consistent with the test, and then giving reasonable parameters, the results can also be very accurate. In addition, by setting a specific program, the PFC can intuitively show when and where the sample will be damaged, and can simulate the damage crack shape through a specific module [45,46].

Unlike other continuous models, PFC software can accurately reveal the basic mechanical behavior of rock-like materials under uniaxial compression, and can intuitively show the fracture evolution process in the sample. When using PFC-3D software to simulate rock-like materials, the contact model between particles usually adopts a parallel bonding model (Figure 14a) [46]. Under axial load, if the local contact force between particles exceeds the shear strength of the contact model, a shear crack will occur between the two particles. In the model, the shear crack is represented by a green circle (Figure 14b). If the local contact force between particles exceeds the tensile strength of the contact model, a tensile crack will occur between the two particles. In the model, the tensile crack is represented by a red circle (Figure 14b).

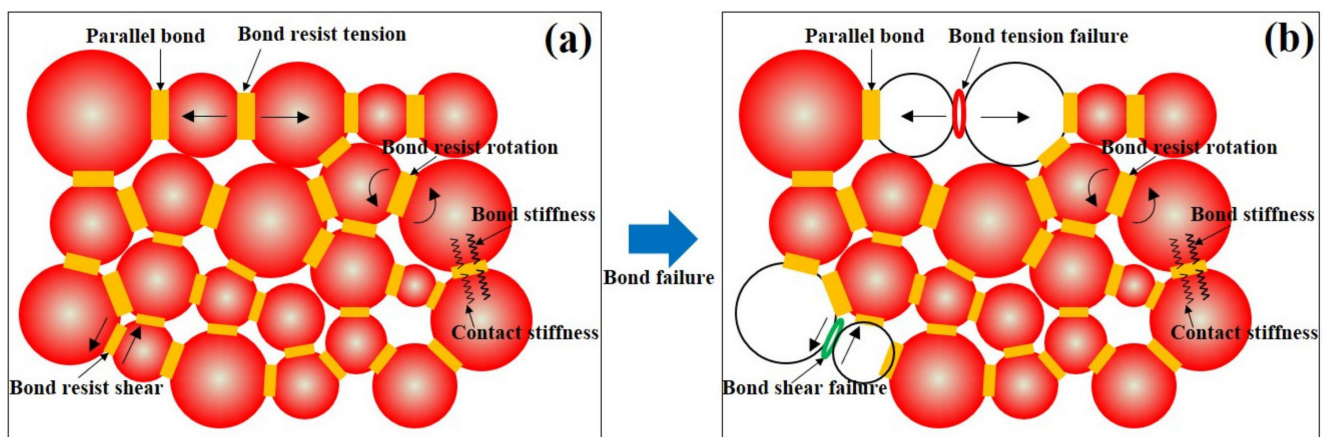


Figure 14. Parallel bonding model: (a) The stress pattern; (b) Failure mode.

The random function in PFC software is used to generate particles with different diameters in the calculation range, and the balance calculation is carried out to make the particles fill the whole columnar calculation range. After the initial equilibrium, a parallel bond model was set for the peripheral rocks and the internal backfill, respectively, and the loading rate of the model was determined. A monitoring system was arranged to monitor the number of cracks, stress and strain of the model in real time. The final stress–strain curve is shown in Figure 9 after multiple corrections of the model’s mesoscopic parameters, and the evolution process of internal cracks in the RBCM sample is finally obtained. The results are shown in Figure 15 (RBCM-10 and RBCM-30). At the initial stage of loading, the local contact force between the RBCM particles is less than its bonding strength, and the stress and strain of the RBCM increase, but there are almost no cracks. With the continued loading of the RBCM, the local contact force between the particles is gradually greater than the bond strength, the bond between some particles is damaged, and cracks are generated. Because the bond strength between the backfill particles is less than that between the rock particles, the cracks first appear between the internal backfill particles. In the middle stage of loading, the bond between most of the backfill particles was destroyed, and the cracks spread all over the backfill. At the same time, the local contact force between rock particles begins to exceed its bond strength, and the cracks begin to appear in the surrounding rocks. In the later stage of loading, the contact force between rock particles is generally greater than its bond strength. The crack evolves on a large scale in the surrounding rock, and gradually forms a macro failure through the crack, which eventually leads to the overall instability and failure of the RBCM.

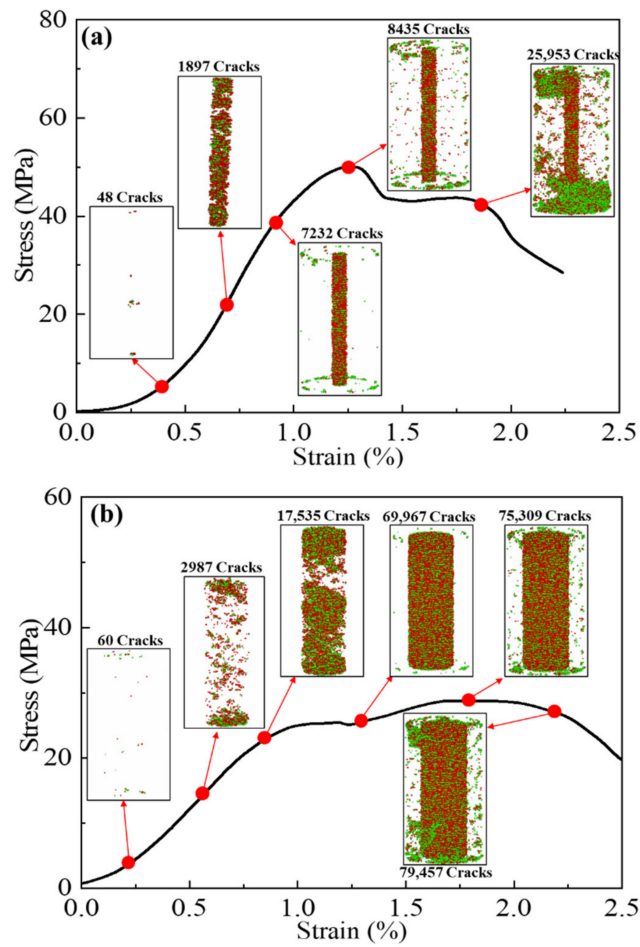


Figure 15. Temporal and spatial evolution of a crack: (a) RBCM-10; (b) RBCM-30.

In order to study the spatial distribution of the internal cracks of the RBCM after compression failure, 10 sections were selected for the numerical model after RBCM model failure, and the results are shown in Figure 16.

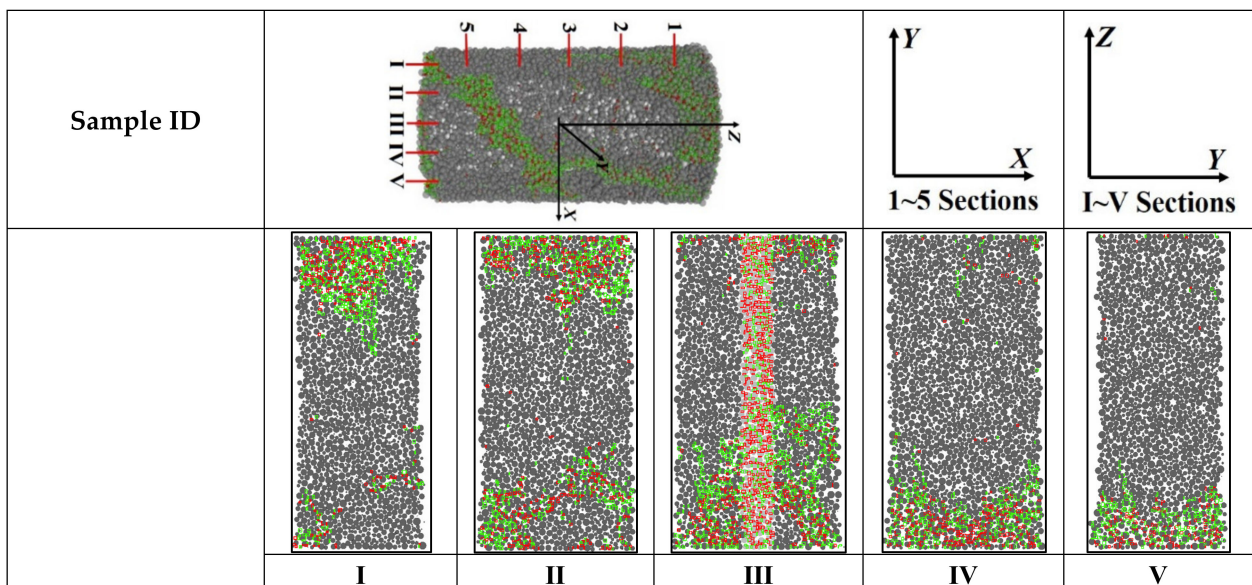


Figure 16. Cont.

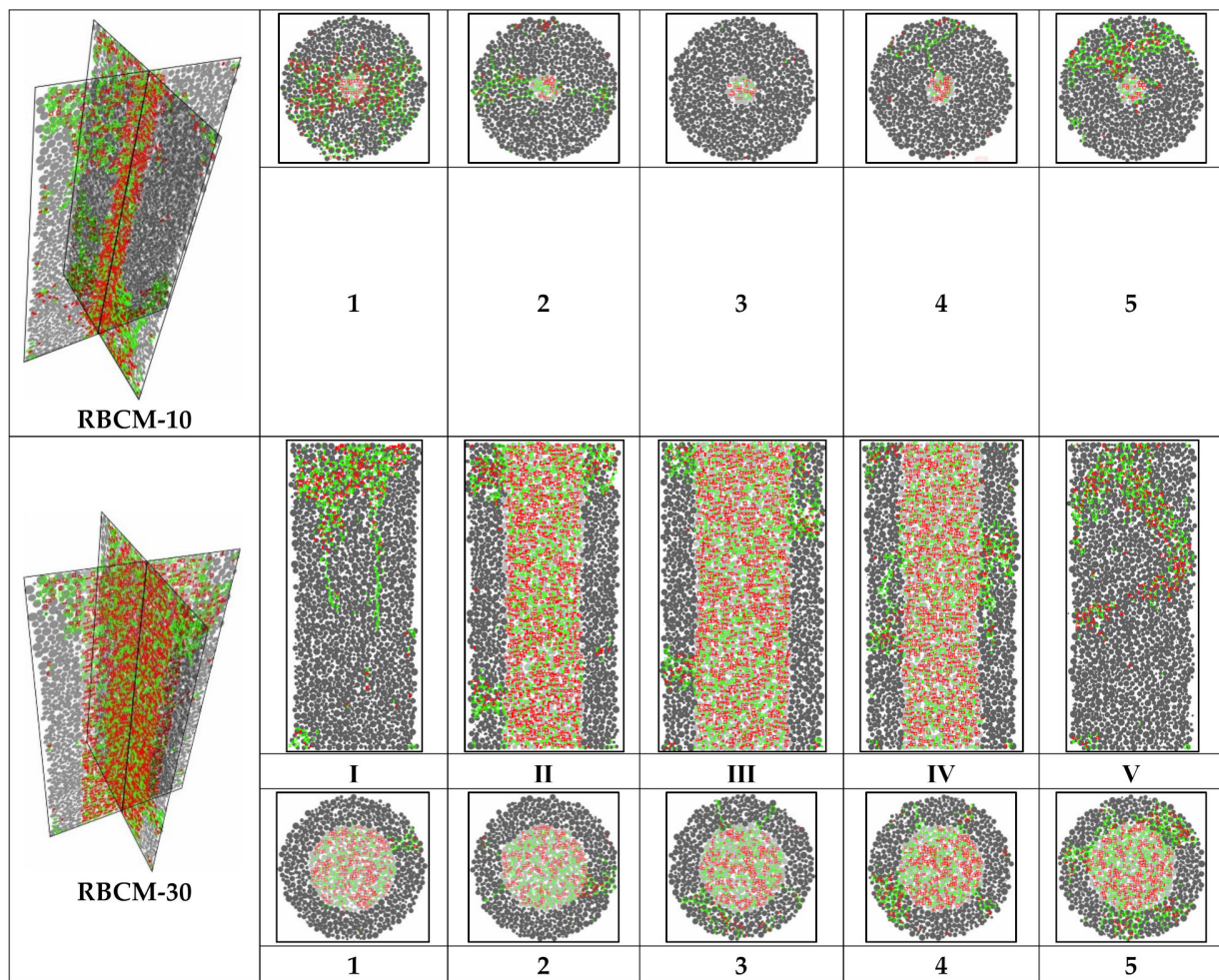


Figure 16. Spatial distribution of the cracks after the samples' failure.

For the RBCM-10, the cracks of section I are mainly distributed at the top of the sample. The cracks of section II are mainly distributed at the upper and lower ends of the sample. Section III contains two parts of rock and backfill; the cracks are mainly distributed in the internal backfill, and some cracks are also distributed at the bottom of the peripheral rock. The cracks of sections IV and V are mainly distributed at the bottom of the sample. In addition, the cracks of sections 1 and 2 are mainly distributed in the internal backfill and the left and right end of the peripheral rock. The cracks of section 3 are mainly distributed in the internal backfill, and there are almost no cracks in the peripheral rock. The cracks of sections 4 and 5 are mainly distributed in the internal backfill and at the top of the peripheral rock. In general, the cracks of RBCM-10 are mainly distributed in the internal backfill and the upper and lower ends of the peripheral rock.

For the RBCM-30, the cracks of sections of I and V are mainly distributed at the top of the rock. The cracks of sections II–IV are mainly distributed in the internal backfill and the top of the peripheral rock. The cracks of sections 1–3 are mainly distributed in the internal backfill, and there are few cracks in the peripheral rock. The cracks of section 4 are mainly distributed in the internal backfill and the left end of the peripheral rock. The cracks of section 5 are mainly distributed in the internal backfill and the upper and lower ends of the peripheral rock. In general, the cracks of the RBCM-30 are mainly distributed in the internal backfill and the top and bottom ends of the peripheral rocks.

Considering the spatial distribution law of cracks in RBCM-10 and RBCM-30, most of the cracks are distributed in the internal backfill, and a few cracks are distributed at the

upper and lower ends of the peripheral rock. The evolution of meso tension cracks and shear cracks in the model leads to macro penetration failure.

4. Discussion

In Section 3.3, the damage evolution equation of the RBCM was established, and the damage evolution characteristics of the RBCM were studied. In Section 3.4, the AE correlation fractal dimension of the RBCM was calculated, and the qualitative relationship between AE correlation fractal dimension, damage evolution characteristics, and strain gradient were analyzed. The analysis results show that the AE correlation fractal dimension is inversely proportional to the strain gradient, while the damage evolution characteristics are directly proportional to the strain gradient. The damage directly represents the evolution process of cracks in the RBCM, and the AE correlation fractal dimension is a summary of the AE parameters released by the RBCM during loading. Therefore, the AE correlation fractal dimension can indirectly represent the damage evolution process of the RBCM to a certain extent. The AE correlation fractal dimension must have some internal relationship with the damage evolution characteristics.

In order to study the internal functional relationship between the AE correlation fractal dimension and damage value, the relationship curve between the AE correlation fractal dimension and damage evolution characteristics was established. The results are shown in Figure 17. The AE correlation fractal dimension is inversely proportional to the damage evolution. This is consistent with the research conclusion of reference [31]. Reference [31] shows that with the increase of stress percentage, the fractal dimension of the CPB decreases under uniaxial stress, while the damage variable of the CPB increases gradually. In addition, the damage variable increases more rapidly. When the fractal dimension decreases to a certain level, the fractal dimension no longer decreases significantly, and the CPB damage variable increases rapidly.

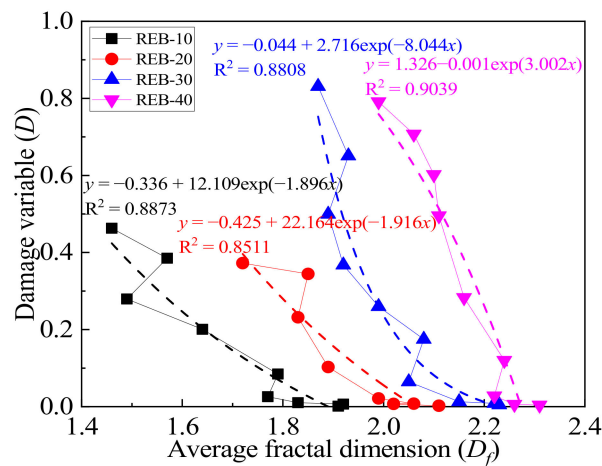


Figure 17. The relationship between the damage variable and the average fractal dimension.

Take the RBCM-20 as an example; when the AE correlation fractal dimension is 1.72, the damage value is 0.37. When the AE correlation fractal dimension increases to 1.85, 1.89, and 2.06, respectively, the damage values decrease to 0.34, 0.10, and 0.01, respectively. A variety of functions are used to fit the relationship between the AE correlation fractal dimension and damage value. The results show that the exponential function can better characterize the relationship between them:

$$D = a_4 + b_4 \cdot \exp(c_4 \cdot D_f) \tag{13}$$

where D is the damage variable of the RBCM, D_f is the AE correlation fractal dimension of the RBCM, and a_4 , b_4 , and c_4 are relevant parameters.

Under the action of a load, the internal stress of the RBCM increases continuously and gradually exceeds the bond strength between the particles. Cracks are generated between the particles, resulting in damage accumulation, and releasing energy to the outside in the form of acoustic emission. Therefore, during compression, stress behavior, damage characteristics, AE events, and microcracks must be interrelated. Figure 18 shows the composite diagram of the stress–strain, damage value, AE event, and cracks of the RBCM-30. When the internal stress of RBCM-30 increases to 4.57 MPa, its damage value evolves to 0.01, the number of microcracks increases to 60, and the AE events are mainly concentrated in the internal backfill. When the internal stress increases to 12.42 MPa, the damage value evolves to 0.02, the number of microcracks increases to 2987, and the AE events accumulate rapidly in the internal backfill. When the internal stress increases to 21.92 MPa, the damage value evolves to 0.06, the number of microcracks increases to 17,535, and the AE event begins to expand from the internal backfill to the surrounding rock. When the internal stress increases to 28.63 MPa, the damage value evolves to 0.34, the number of microcracks increases to 75,309, and the increment of the microcracks is the largest at this stage; the AE events accumulate rapidly in the surrounding rocks. When the internal stress reaches the peak and decreases to 26.83 MPa, the damage value evolves to 0.65, the number of microcracks increases slightly to 79,457, and the AE events increase slightly in the whole sample.

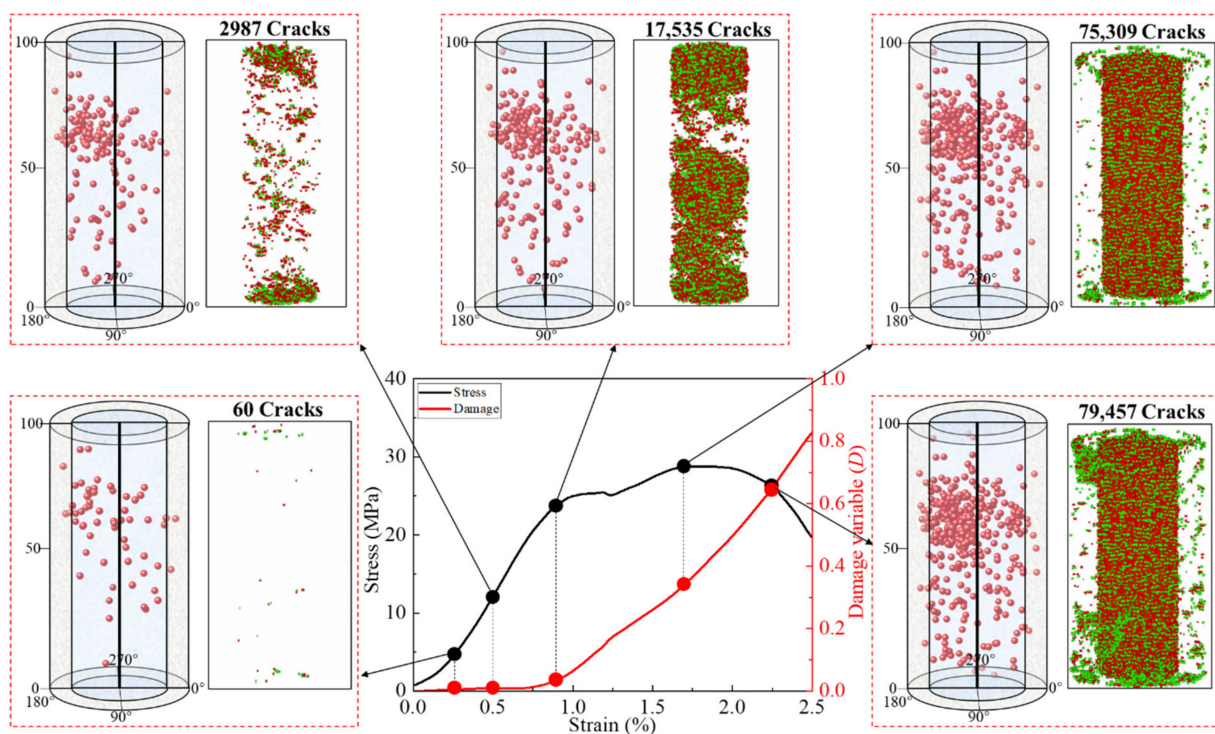


Figure 18. The composite diagram of the stress, damage, AE events, and cracks of the RBCM-30.

5. Conclusions

In this paper, firstly, the macroscopic mechanical behavior of the RBCM was analyzed, and the damage constitutive model of the RBCM was established. Secondly, the AE ring counting correlation fractal dimension was deduced. Finally, with the help of PFC software, the microcrack distribution was dynamically displayed. The main conclusions are as follows:

- (1) The stress–strain curve of the RBCM can be divided into five stages: the pore compaction closure stage, the linear elasticity stage, the yield stage, the peak strength stage, and the residual stress stage; some stress–strain curves show double peaks. The σ^p , ε^p , and E decreased with the increase of the internal backfill diameter.

- (2) The U^T shows an S-shaped distribution. The U^E shows an inverted U-shaped distribution. The U^D first increases slowly and then increases rapidly. The U_p^T , U_p^E , and U_p^D all decrease with the increase of the backfill diameter. The U_p^E/U_p^D and U_p^E/U_p^T decrease and the U_p^D/U_p^T increases with the increases of the backfill diameter.
- (3) A damage constitutive model of the RBCM was established. The damage evolution curves and damage rate evolution curves of the RBCM show S-shaped and U-shaped distributions, respectively.
- (4) The AE correlation fractal dimension of the RBCM was deduced and calculated. The AE correlation fractal dimension decreases with the increase of the strain gradient and damage value, and the AE correlation fractal dimension presents a linear and an exponential function with them, respectively. The AE events' localization results show that the damage first accumulates in the internal backfill. Then, the damage extends into the surrounding rock. Finally, the damage accumulates rapidly in the surrounding rock.
- (5) The internal microcracks of the RBCM are caused by the local tensile stress or shear stress between particles exceeding the bond strength between particles. With the increase of stress, microcracks first appear and gather in the internal backfill of the RBCM, and then microcracks also appear and gather in the peripheral rock, which together leads to the macro penetration failure of the RBCM.

Author Contributions: Conceptualization, J.W. and W.S.; methodology, C.Z.; software, J.W.; validation, Y.Z.; formal analysis, Y.Z.; investigation, C.Z.; resources, W.S.; data curation, J.W.; writing—original draft preparation, C.Z.; writing—review and editing, J.W.; visualization, J.W.; supervision, Y.Z.; project administration, W.S.; funding acquisition, W.S. All authors have read and agreed to the published version of the manuscript.

Funding: This experimental work was financially supported by the National Natural Science Foundation of China (Grant No. 51974012), the National Natural Science Foundation of China Youth Fund (51804016), and the China Postdoctoral Science Foundation (2021M690361).

Acknowledgments: The experimental works described in this study were conducted at the Key Laboratory of High-Efficient Mining and Safety of Metal Mines of the Ministry of Education in the University of Science and Technology Beijing. The authors gratefully acknowledge the staff and students at the laboratory for their technical help during the testing.

Conflicts of Interest: The authors declare no conflict of interest.

References

1. Wang, J.; Fu, J.; Song, W. Mechanical properties and microstructure of layered cemented paste backfill under triaxial cyclic loading and unloading. *Constr. Build. Mater.* **2020**, *257*, 119540. [[CrossRef](#)]
2. Wang, J.; Fu, J.; Song, W.; Zhang, Y.; Wu, S. Acoustic emission characteristics and damage evolution process of layered cemented tailings backfill under uniaxial compression. *Constr. Build. Mater.* **2021**, *295*, 123663. [[CrossRef](#)]
3. Xu, W.; Cao, Y.; Liu, B. Strength efficiency evaluation of cemented tailings backfill with different stratified structures. *Eng. Struct.* **2019**, *180*, 18–28. [[CrossRef](#)]
4. Xu, W.-B.; Liu, B.; Wu, W.-L. Strength and deformation behaviors of cemented tailings backfill under triaxial compression. *J. Central South Univ.* **2020**, *27*, 3531–3543. [[CrossRef](#)]
5. Wang, J.; Fu, J.; Song, W.; Zhang, Y. Viscosity and Strength Properties of Cemented Tailings Backfill with Fly Ash and Its Strength Predicted. *Minerals* **2021**, *11*, 78. [[CrossRef](#)]
6. Ferdi, C.; Yunus, A.; Marco, C. Effect of Desliming of Tailings on the Fresh and Hardened Properties of Paste Backfill Made from Alkali-Activated Slag. *Adv. Mater. Sci. Eng.* **2020**, *2020*, 4536257.
7. Hou, J.; Guo, Z.; Li, J.; Zhao, L. Study on triaxial creep test and theoretical model of cemented gangue-fly ash backfill under seepage-stress coupling. *Constr. Build. Mater.* **2021**, *273*, 121722. [[CrossRef](#)]
8. Xiu, Z.; Wang, S.; Ji, Y.; Wang, F.; Ren, F.; Nguyen, V.-T. Loading rate effect on the uniaxial compressive strength (UCS) behavior of cemented paste backfill (CPB). *Constr. Build. Mater.* **2021**, *271*, 121526. [[CrossRef](#)]
9. Zhao, K.; Yu, X.; Zhu, S.T.; Zhou, Y.; Wang, Q.; Wang, J.Q. Acoustic emission investigation of cemented paste backfill pre-prepared with tantalum-niobium tailings. *Constr. Build. Mater.* **2020**, *237*, 117523. [[CrossRef](#)]
10. Doherty, J.P.; Wood, D.M. A bonding and damage constitutive model for lightly cemented granular material. *Comput. Geotech.* **2020**, *127*, 103732. [[CrossRef](#)]

11. Dzaye, E.D.; De Schutter, G.; Aggelis, D.G. Monitoring early-age acoustic emission of cement paste and fly ash paste. *Cem. Concr. Res.* **2020**, *129*, 105964. [[CrossRef](#)]
12. Sun, Q.; Li, B.; Tian, S.; Cai, C.; Xia, Y. Creep properties of geopolymer cemented coal gangue-fly ash backfill under dynamic disturbance. *Constr. Build. Mater.* **2018**, *191*, 644–654. [[CrossRef](#)]
13. Li, H.; Wu, A.; Wang, H. Evaluation of short-term strength development of cemented backfill with varying sulphide contents and the use of additives. *J. Environ. Manag.* **2019**, *239*, 279–286. [[CrossRef](#)]
14. Fang, K.; Fall, M. Insight into the mode I and mode II fracture toughness of the cemented backfill-rock interface: Effect of time, temperature and sulphate. *Constr. Build. Mater.* **2020**, *262*, 120860. [[CrossRef](#)]
15. Fang, K.; Cui, L.; Fall, M. A coupled chemo-elastic cohesive zone model for backfill-rock interface. *Comput. Geotech.* **2020**, *125*, 103666. [[CrossRef](#)]
16. Koupouli, N.J.; Belem, T.; Rivard, P.; Effenguet, H. Direct shear tests on cemented paste backfill–rock wall and cemented paste backfill–backfill interfaces. *J. Rock Mech. Geotech. Eng.* **2016**, *8*, 472–479. [[CrossRef](#)]
17. Wang, Y.R.; Lu, H.J.; Wu, J. Experimental investigation on strength and failure characteristics of cemented paste back-fill-rock composite under uniaxial compression. *Constr. Build. Mater.* **2021**, *304*, 124629. [[CrossRef](#)]
18. Wu, W.L.; Xu, W.B.; Zuo, J.P. Effect of inclined interface angle on shear strength and deformation response of cemented paste backfill-rock under triaxial compression. *Constr. Build. Mater.* **2021**, *279*, 122478.
19. Xiu, Z.; Wang, S.; Ji, Y.; Wang, F.; Ren, F.; Nguyen, V.-T. The effects of dry and wet rock surfaces on shear behavior of the interface between rock and cemented paste backfill. *Powder Technol.* **2021**, *381*, 324–337. [[CrossRef](#)]
20. Zhao, L. Numerical investigation on the mechanical behaviour of combined backfill-rock structure with KCC model. *Constr. Build. Mater.* **2021**, *283*, 122782. [[CrossRef](#)]
21. Yu, X.; Kemeny, J.; Tan, Y.; Song, W.; Huang, K. Mechanical properties and fracturing of rock-backfill composite specimens under triaxial compression. *Constr. Build. Mater.* **2021**, *304*, 124577. [[CrossRef](#)]
22. Wang, J.; Fu, J.X.; Song, W.D.; Zhang, Y.F.; Wang, Y. Mechanical behavior, acoustic emission properties and damage evolution of cemented paste backfill considering structural feature. *Constr. Build. Mater.* **2010**, *261*, 119958. [[CrossRef](#)]
23. Shah, S.G.; Kishen, J.M.C. Fracture behavior of concrete-concrete interface using acoustic emission technique. *Eng. Fract. Mech.* **2010**, *77*, 908–924. [[CrossRef](#)]
24. Liu, S.; Li, X.; Li, Z.; Chen, P.; Yang, X.; Liu, Y. Energy distribution and fractal characterization of acoustic emission (AE) during coal deformation and fracturing. *Measurement* **2019**, *136*, 122–131. [[CrossRef](#)]
25. Anay, R.; Soltangharaei, V.; Assi, L.; DeVol, T.; Ziehl, P. Identification of damage mechanisms in cement paste based on acoustic emission. *Constr. Build. Mater.* **2018**, *164*, 286–296. [[CrossRef](#)]
26. Hou, Y.; Yin, S.; Chen, X.; Zhang, M.; Yang, S. Study on characteristic stress and energy damage evolution mechanism of cemented tailings backfill under uniaxial compression. *Constr. Build. Mater.* **2021**, *301*, 124333. [[CrossRef](#)]
27. Wang, J.; Song, W.; Cao, S.; Tan, Y. Mechanical properties and failure modes of stratified backfill under triaxial cyclic loading and unloading. *Int. J. Min. Sci. Technol.* **2019**, *29*, 809–814. [[CrossRef](#)]
28. Song, W.D.; Wang, J.; Tan, Y.Y.; Cao, S. Energy consumption and damage characteristics of stratified backfill under triaxial loading and unloading. *J. China Univ. Min. Technol.* **2017**, *45*, 1050–1057.
29. Xin, L. Meso-scale modeling of the influence of waste rock content on mechanical behavior of cemented tailings backfill. *Constr. Build. Mater.* **2021**, *307*, 124473. [[CrossRef](#)]
30. Zhao, K.; Yu, X.; Zhu, S.; Yan, Y.; Zhou, Y.; He, Z.; Song, Y.; Huang, M. Acoustic emission fractal characteristics and mechanical damage mechanism of cemented paste backfill prepared with tantalum niobium mine tailings. *Constr. Build. Mater.* **2020**, *258*, 119720. [[CrossRef](#)]
31. Zhou, Y.; Yan, Y.; Zhao, K.; Yu, X.; Song, Y.; Wang, J.; Suo, T. Study of the effect of loading modes on the acoustic emission fractal and damage characteristics of cemented paste backfill. *Constr. Build. Mater.* **2021**, *277*, 122311. [[CrossRef](#)]
32. He, Z.; Zhao, K.; Yan, Y.; Ning, F.; Zhou, Y.; Song, Y. Mechanical response and acoustic emission characteristics of cement paste backfill and rock combination. *Constr. Build. Mater.* **2021**, *288*, 123119. [[CrossRef](#)]
33. Wang, J.; Fu, J.; Song, W.; Zhang, Y. Mechanical properties, damage evolution, and constitutive model of rock-encased backfill under uniaxial compression. *Constr. Build. Mater.* **2021**, *285*, 122898. [[CrossRef](#)]
34. Ma, Q.; Tan, Y.; Liu, X.; Gu, Q.; Li, X. Effect of coal thicknesses on energy evolution characteristics of roof rock-coal-floor rock sandwich composite structure and its damage constitutive model. *Compos. Part B Eng.* **2020**, *198*, 108086. [[CrossRef](#)]
35. Liu, W.Z.; Chen, J.T.; Guo, Z.P.; Yang, H.Z.; Xie, W.W.; Zhang, Y.D. Mechanical properties and damage evolution of cemented coal gangue-fly ash backfill under uniaxial compression: Effects of different curing temperatures. *Constr. Build. Mater.* **2021**, *305*, 124820. [[CrossRef](#)]
36. Cui, L.; Fall, M. An evolutive elasto-plastic model for cemented paste backfill. *Comput. Geotech.* **2016**, *71*, 19–29. [[CrossRef](#)]
37. Zhou, Y.; Yu, X.; Guo, Z.; Yan, Y.; Zhao, K.; Wang, J.; Zhu, S. On acoustic emission characteristics, initiation crack intensity, and damage evolution of cement-paste backfill under uniaxial compression. *Constr. Build. Mater.* **2021**, *269*, 121261. [[CrossRef](#)]
38. Qiu, J.; Zhou, Y.; Vatin, N.I.; Guan, X.; Sultanov, S.; Khemarak, K. Damage constitutive model of coal gangue concrete under freeze-thaw cycles. *Constr. Build. Mater.* **2020**, *264*, 120720. [[CrossRef](#)]
39. Liu, X.S.; Tan, Y.L.; Ning, J.G.; Lu, Y.W.; Gu, Q.H. Mechanical properties and damage constitutive model of coal in coal-rock combined body. *Int. J. Rock Mech. Min. Sci.* **2018**, *110*, 140–150. [[CrossRef](#)]

40. Fu, J.; Wang, J.; Song, W. Damage constitutive model and strength criterion of cemented paste backfill based on layered effect considerations. *J. Mater. Res. Technol.* **2020**, *9*, 6073–6084. [[CrossRef](#)]
41. Xie, H.P.; Ju, Y.; Li, L.Y. Criteria for strength and structural failure of rocks based on energy dissipation and energy release principles. *Chin. J. Rock Mech. Eng.* **2005**, *24*, 3003–3010.
42. Jia, Z.Q.; Li, C.B.; Zhang, R.; Wang, M.; Gao, M.Z.; Zhang, Z.T.; Zhang, Z.P.; Ren, L.; Xie, J. Energy Evolution of Coal at Different Depths Under Unloading Conditions. *Rock Mech. Rock Eng.* **2019**, *52*, 4637–4649. [[CrossRef](#)]
43. Guo, H.F.; Song, D.Z.; He, X.Q.; Lou, Q.; Qiu, L.M. Fractal characteristics of acoustic emission in different damage degrees of impact coal. *Coal Sci. Technol.* **2021**, *49*, 38–46.
44. Gong, C.; Zhao, K.; Bao, H.; Zhao, K.; Zeng, P.; Wang, W.J. Acoustic emission source evolution characteristics and fractal features during creep failure of red sandstone. *Rock Soil Mech.* **2021**, *42*, 1–13.
45. Wang, J.; Fu, J.X.; Song, W.D.; Zhang, Y.F.; Wang, Y. Particle flow simulation of mechanical properties and microcrack evolution characteristics of rock-backfill combined model. *J. China Univ. Min. Technol.* **2020**, *49*, 453–462.
46. Cheng, A.; Shu, P.; Deng, D.; Zhou, C.; Huang, S.; Ye, Z. Microscopic acoustic emission simulation and fracture mechanism of cemented tailings backfill based on moment tensor theory. *Constr. Build. Mater.* **2021**, *308*, 125069. [[CrossRef](#)]